

Compton imaging of undepleted volumes of germanium detectors

Iris Abt¹ , Arthur Butorev¹ , Felix Hagemann^{1,4,a} , David Hervas Aguilar^{1,2,3,5} ,
Johanna Lührs^{1,6} , Julia Penner^{1,5} , Oliver Schulz¹ 

¹Max-Planck-Institut für Physik, Boltzmannstraße 8, 85748 Garching bei München, Germany

²University of North Carolina, Department of Physics and Astronomy, 120 E. Cameron Ave., Phillips Hall CB3255, Chapel Hill, 27599 NC, USA

³Triangle Universities Nuclear Laboratory, 116 Science Drive, Duke University, Durham, 27708 NC, USA

⁴Present Address: Space Sciences Laboratory, University of California, Berkeley, 7 Gauss Way, Berkeley CA 94720, USA

⁵Present Address: Department of Physics, TUM School of Natural Sciences, Technical University of Munich, James-Franck-Straße 1, 85748 Garching bei München, Germany

⁶Present Address: Max-Planck-Institut für Kernphysik, Saupfercheckweg 1, 69117 Heidelberg, Germany

Received: date / Accepted: date

Abstract The shape of the undepleted volume of a p-type high-purity Broad Energy Germanium detector, dependent on the bias voltage, has been imaged by measuring spatially-resolved Compton-scattering efficiency. The bias voltage was raised stepwise from -50 V to the full-depletion voltage. The geometric acceptance was determined at full depletion. Below full depletion, the relative acceptance observed for $2 \times 2 \times 2\text{ mm}^3$ voxels was used to create the image of the undepleted volume for each bias voltage. The images were used to extract the impurity density profile of the detector by fitting predictions of the open-source software package *SolidState-Detectors.jl* to the images. The result is shown and compared to the impurity density profile deduced from capacitance measurements. This is the first time that three-dimensional images of the undepleted volumes of a germanium detector have become available and have been used to deduce an impurity density profile.

1 Introduction

High-purity germanium detectors are well known for their efficiency in detecting gamma rays with excellent energy resolution. This is sufficient for many applications in industry and research. However, for rare-event searches like the search for neutrinoless double-beta decay [1–3] or for dark matter [4–6], more information is needed. Additional information is deduced from the shape of the charge pulse produced by a germanium detector in response to the interaction of a particle with the crystal. This so-called pulse shape analysis is used to separate signal events from background and relies strongly on verification from comparisons between measured and simulated pulses. Thus, the basic physics in-

side a germanium detector as well as the parameters of the simulated detector have to be extremely well understood.

In order to operate a germanium detector, a bias voltage, V_B , is applied to the contacts of the detector to generate an electric field inside the detector. This field has two functions:

1. It separates the electrons and holes produced by particle interactions; this process generates the desired signal.
2. It sweeps out the free charge carriers produced inside the crystal by the impurities; this process is called depletion, during which the electrically active impurities are ionized.

These ionized impurities also affect the electric field.

A detector is fully operational when it is depleted throughout its volume. This happens for V_B above the so-called full-depletion voltage, V_D . For lower V_B , the detector is expected to have efficient charge collection only in the depleted volume.

The simulation of the pulses of a detector requires a realistic calculation of the electric field. This, in turn, requires the impurity density profile of the detector as an important input. However, the impurity density profile is *a priori* not well known. The manufacturer typically provides impurity values at the top and the bottom of the crystal, usually obtained via Hall measurements. Moreover, there is a 20% uncertainty associated with these impurity density measurements [7]. In general, no radial dependence is assumed. The values of V_D as calculated based on the provided impurity density values and a linear interpolation between them often do not match the observed values of V_D . In addition, some radial dependencies of the impurity density have been observed lately [8–10].

As the evolution of the undepleted volume with increasing V_B depends on the impurity density profile, the observation of the way the undepleted volume shrinks can be used to obtain information about the impurity density profile.

In this paper, we present a way to directly image the undepleted volume inside a germanium detector using the Comp-

^ae-mail: hagemann@mpp.mpg.de (corresponding author)

ton Scanner [11] at the Max-Planck-Institute for Physics. Also presented is an analysis of the images to extract the impurity density profile. It is shown that a radial dependence of the impurity density profile is needed to explain the images. This result is compared to results obtained from capacitance measurements. The paper closes with suggestions on how germanium detectors should be characterized before being deployed in large experiments.

2 The p-type segBEGe detector

The detector used for this study was a p-type segmented Broad Energy Germanium (segBEGe) detector, manufactured by Mirion Technologies. It was a cylindrical detector with a diameter of 74.5 mm and a height of 39.5 mm, see Fig. 1. The p^+ point contact on top of the detector, the so-called core contact, was a Boron implant. It had a diameter of 15 mm and was surrounded by a passivated ring with an outer diameter of 39 mm. The bottom, side and outer part of the top surface of the detector were covered with a four-fold segmented Lithium-drifted n-type contact. The thickness of the Lithium contact at the side of the detector was measured in radial scans to be 0.75 ± 0.06 mm [12, p. 123]. The smaller segments 1, 2 and 3 each extended over 60° , while segment 4 covered the remaining surface on the top and side of the detector and had a closed bottom end-plate. However, the segmentation is not important for the analyses presented in this paper because the contacts were grounded and the detector was effectively a BEGe detector.

Figure 1a also depicts the cylindrical coordinate system, r , φ and z , used to describe positions in the detector. The origin of the coordinate system is located in the center of the bottom surface of the detector. The segment boundary between segment 1 and 4 which was closer to segment 3 defines $\varphi = 0^\circ$. The bottom surface of the detector defines $z = 0$ mm with the z -values increasing towards the top of the detector at $z = 39.5$ mm.

The detector manufacturer [13] reported the net impurity density of the p-type segBEGe detector to be 12.1 % higher at the top, i.e. $\rho_{\text{top}} = -6.5 \cdot 10^9 \text{ cm}^{-3}$, compared to at the bottom of the detector, i.e. $\rho_{\text{bot}} = -5.8 \cdot 10^9 \text{ cm}^{-3}$. The calculation using these values for the impurity densities, assuming a linear z -dependence¹ and no radial dependence, predicted a value of $V_D = -1437$ V. To reproduce the lower measured value of $V_D = -1275$ V [12], the impurity density values had to be scaled down to 89 %. The standard operating voltage was -3000 V to assure efficient charge collection.

The calculated electric potential and electric field inside the detector is presented in Fig. 2 and explained in section 4.

¹For the moderate height of 39.5 mm and the relatively low difference of 12.1 %, the assumption of linearity is reasonable. For higher detectors or larger differences between top and bottom, this might not be the case and better models might be needed [14].

3 Experimental setup

The measurements for this paper were taken with the fully automated Compton Scanner [11] shown in Fig. 3. The setup was developed and operated at the Max-Planck-Institute for Physics to characterize the bulk of germanium detectors. It relies on reconstructing interaction positions from single-Compton-scatter events measured in coincidence with surrounding pixelated cameras, which allows pulse shapes from individual events to be associated with their spatial origin.

The p-type segBEGe detector was cooled to 78 K in the temperature-controlled cryostat K2 [12, p. 69] placed at the center of the Compton Scanner. The detector was biased by grounding all segment contacts and applying the negative potential V_B to the core contact. The charges induced on the core contact were amplified using a charge-sensitive preamplifier and recorded using the STRUCK SIS3316-250-14 analog-to-digital converter with a sampling time of 4 ns and a 14 bit resolution.

The detector was irradiated with a collimated beam of 661.66 keV gammas from a 740 MBq ^{137}Cs source. The beam spot diameter at the top (bottom) of the detector was 1.23 mm (1.61 mm) for all radii, resulting in an average size of the beam spot of 1.40 mm. A system of motors was used to place the source at any position above the detector with a precision of better than 100 μm .

The gammas from Compton scattering events were detected by a pixelated camera system at the side of the detector. Events were selected if the germanium detector and the pixelated cameras detected energies in coincidence, adding up to the characteristic energy of 661.66 keV within a window of ± 50 keV. The x and y position of the Compton scatter was defined by the position of the ^{137}Cs source. The z position was reconstructed from the source position, the energy ratio between detector and camera and the position of the Compton scattered gamma in the camera. Full details about the position reconstruction algorithm are reported in Ref. [11]. However, this simple reconstruction is only valid for events with a single Compton scatter in the germanium detector. This single-scatter hypothesis can be validated if the camera registers two hits, i.e. the scattered gamma reaching the camera Compton scatters again in the camera before being photo-absorbed. Only validated events, i.e. with two hits in the camera, were considered for the analysis presented in this paper. A further benefit of the validation requirement is that the z position of the scatter in the detector can be determined without using the energy measured by the detector. This is important for measurements at low V_B , where the energy resolution of the detector degrades.

The special feature of the Compton Scanner is that it can probe all z positions in a detector simultaneously. This is what makes investigations of large volumes of the bulk feasible by keeping scan times manageable.

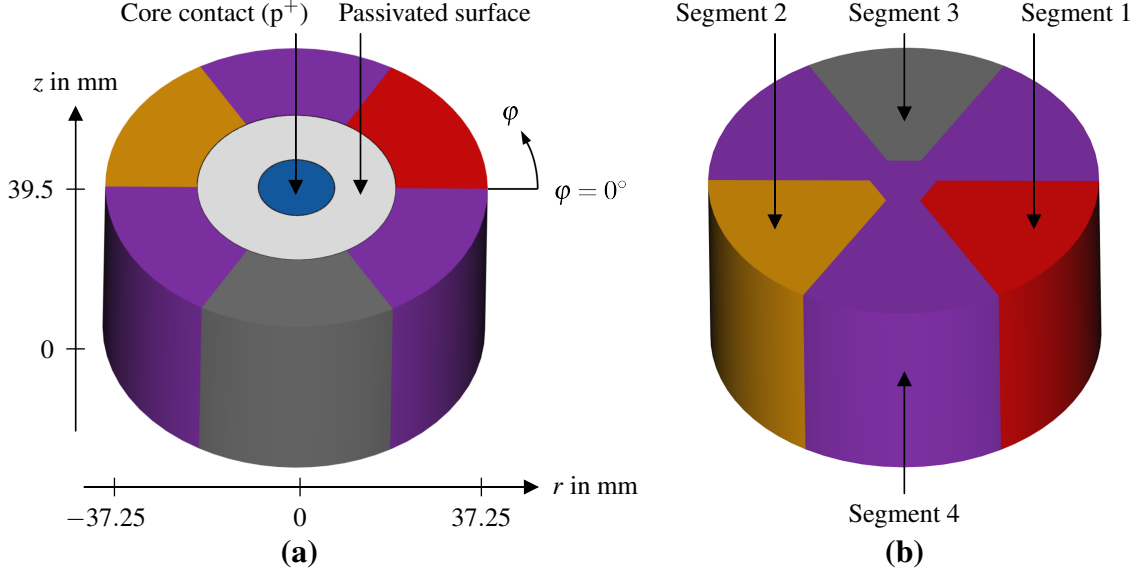


Fig. 1 Schematic of the p-type segBEGe detector: (a) top view and (b) bottom view. In (a), the cylindrical coordinate system to describe positions in the segBEGe detector is shown. The segments had Lithium-drifted contacts which were grounded for the data taken for this paper.

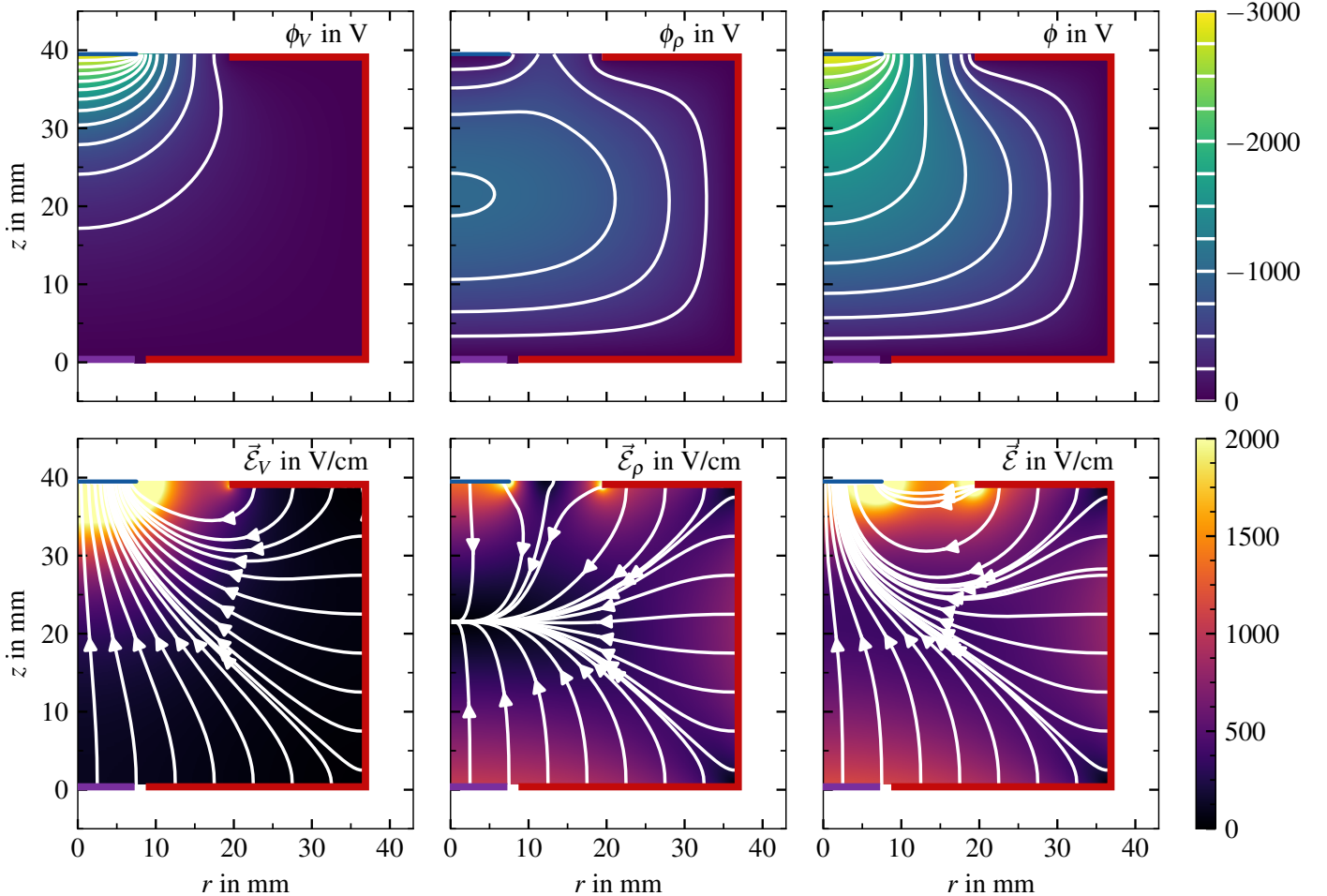


Fig. 2 Top row: electric potential in the r - z -plane at $\varphi = 30^\circ$ resulting from (left) applying just the potentials to the contacts, ϕ_V , (center) just the charge density from ionized impurities, ϕ_ρ and (right) total electric potential, ϕ . The white lines depict equipotential lines at integer multiples of -250 V. Bottom row: corresponding electrical fields. The white lines represent field lines.

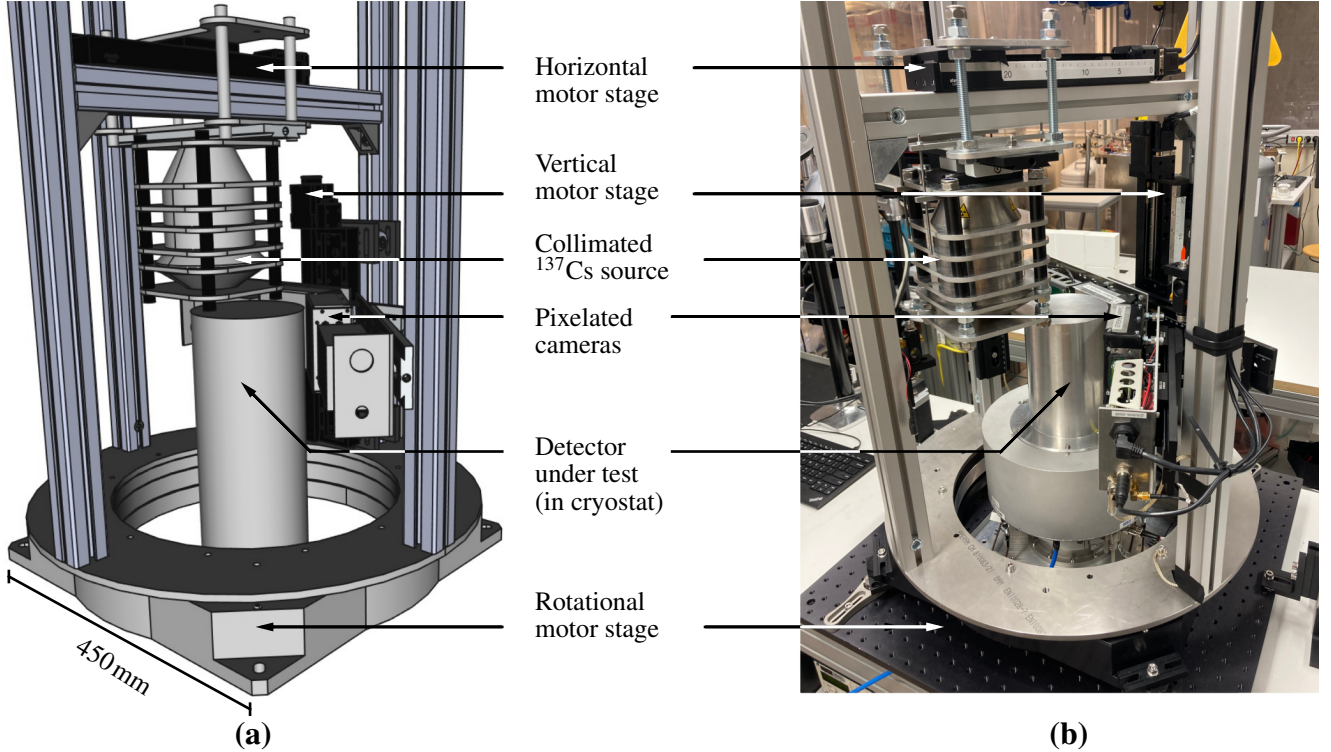


Fig. 3 (a) Drawing of the Compton Scanner, (b) photo of the setup. A second camera provided an increased acceptance compared to the original setup [11].

4 Simulation framework

All potential and field calculations for this paper were performed with the open-source **julia** simulation software package *SolidStateDetectors.jl* [15].

SolidStateDetectors.jl performs 3D and 2D calculations of the electric potential inside the germanium detector using a successive over-relaxation algorithm on an adaptive grid with red-black division, which allows efficient and parallel execution. Whenever possible, 2D simulations were used. In all cases, a cross-check was performed to assure that there was no significant difference between the results for 3D and 2D calculations.

The electric potential, $\phi(\vec{r})$, inside the detector is calculated using Gauss's law, i.e.

$$\nabla \cdot (\epsilon_r(\vec{r}) \nabla \phi(\vec{r})) = -\frac{\rho(\vec{r})}{\epsilon_0}, \quad \text{with } \phi(\vec{r})|_{S_i} = \phi_i, \quad (1)$$

where $\rho(\vec{r})$ is the density of space charge originating from ionized impurities², $\epsilon_0 = 8.854 \cdot 10^{-12} \text{ F/m}$ is the dielectric constant, $\epsilon_r(\vec{r})$ is the relative permittivity of the material at position \vec{r} , e.g. 16 for germanium. The boundary conditions denote that a potential ϕ_i is applied to the contact S_i , where i is the index of the contact. For the data presented in this paper, $\phi_i = 0 \text{ V}$ for all segments.

²We did not consider any charge accumulation on surfaces as it does not influence the bulk volumes discussed in this paper.

The overall potential $\phi(\vec{r})$ can be expressed as a sum of two components,

$$\phi(\vec{r}) = \phi_V(\vec{r}) + \phi_\rho(\vec{r}), \quad (2)$$

where $\phi_V(\vec{r})$ and $\phi_\rho(\vec{r})$ denote the contribution of the applied potentials and the ionized impurities, respectively:

$$\nabla \cdot (\epsilon_r(\vec{r}) \nabla \phi_V(\vec{r})) = 0, \quad \text{with } \phi_V(\vec{r})|_{S_i} = \phi_i, \quad (3)$$

$$\nabla \cdot (\epsilon_r(\vec{r}) \nabla \phi_\rho(\vec{r})) = -\frac{\rho(\vec{r})}{\epsilon_0}, \quad \text{with } \phi_\rho(\vec{r})|_{S_i} = 0. \quad (4)$$

The electric potential $\phi(\vec{r})$ of the detector, as well as the two components $\phi_V(\vec{r})$ and $\phi_\rho(\vec{r})$ are shown in Fig. 2. The resulting electrical fields are also shown. The $\phi_\rho(\vec{r})$ component is dominant at the bottom and side of the detector. At the top, the situation also changes significantly by $\phi_\rho(\vec{r})$, which counteracts $\phi_V(\vec{r})$ and, thus, essentially weakens the electric field close to the point contact. This demonstrates how important the knowledge of the impurity density in these volumes is to understand the pulses coming from the detector.

During the calculation of the electric potential, *SolidStateDetectors.jl* also determines the undepleted volume of the detector [12, p. 55]. For a fully depleted detector, no local maxima or minima are observed in the bulk of the detector. If the potential of any grid point is smaller (bigger) than the minimum (maximum) of the potential of all neighboring grid points, the associated volume is marked as undepleted and the charge density induced by ionized impurities is scaled

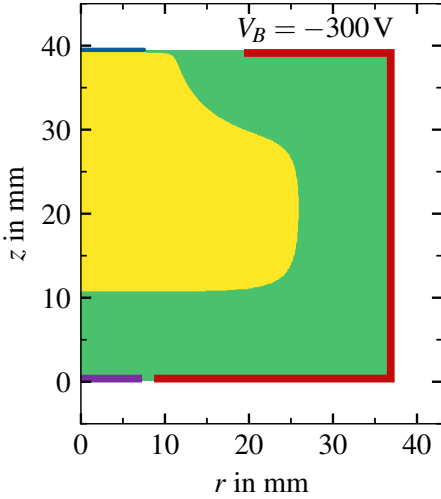


Fig. 4 Simulated undepleted volume (yellow) of the p-type segBEGe detector at $V_B = -300$ V, using the default manufacturer values for the impurity density scaled to 89 % and a thickness of the Lithium-drifted contacts of 0.75 mm.

down until this is no longer the case. This results in an individual scaling factor f for all grid points in the undepleted volume. This is done in each iteration of the calculation of the potential until it converges towards a steady state, in which the potential becomes constant in the undepleted volume.

As an example, Fig. 4 shows the extent of the undepleted volume of the detector as determined for $V_B = -300$ V, using the values of the impurity density as provided by the manufacturer scaled to 89 % and assuming a thickness of 0.75 mm for the Lithium-drifted contact. The lower edge of the undepleted volume in z is mostly determined by the z profile of the impurity density profile. It was investigated that it is not very sensitive to deviations from the linear dependence assumed. Such deviations also do not change the r -extension significantly. The depleted volume evolves from the p-n junction at the segment contacts towards the bulk of the detector. The undepleted volume shrinks as V_B increases and, for this detector, is always connected to the core contact.

5 Compton images

Figure 5 shows the positions of the source, at which data were taken with the Compton Scanner along the $\langle 110 \rangle$ axis in segment 3, starting at $r = 0$ mm and ending at $r = 34$ mm.

The event rates in counts/minute for voxels of 2 mm in z and r for the standard operational V_B of -3000 V are shown in Fig. 6. The voxel size of $2 \times 2 \times 2$ mm 3 reflects the intrinsic spatial resolution of the Compton Scanner of ± 1 mm FWHM in z [11] and the full diameter of the beam spot in the x - y -plane. The overall rates are low due to the requirement of two hits in the cameras. The rates are lower at the bottom than at the top of the detector because of the absorption of incoming gammas. The exponential decrease of the rate from

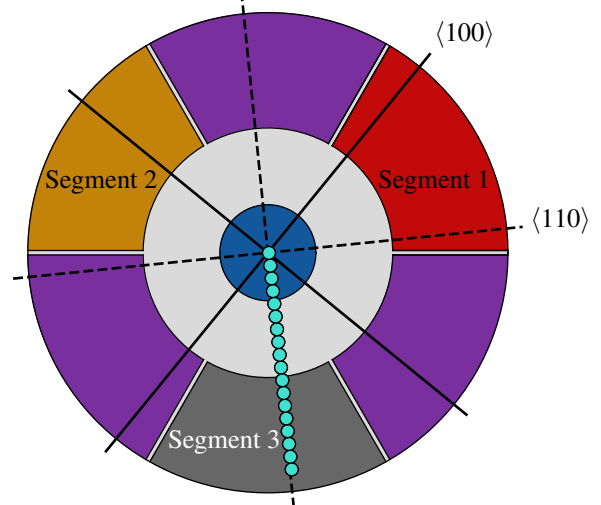


Fig. 5 Top view of the scan points used to image the undepleted volume of the p-type segBEGe detector. The solid and dashed black lines indicate the locations of the $\langle 100 \rangle$ and $\langle 110 \rangle$ axes, respectively.

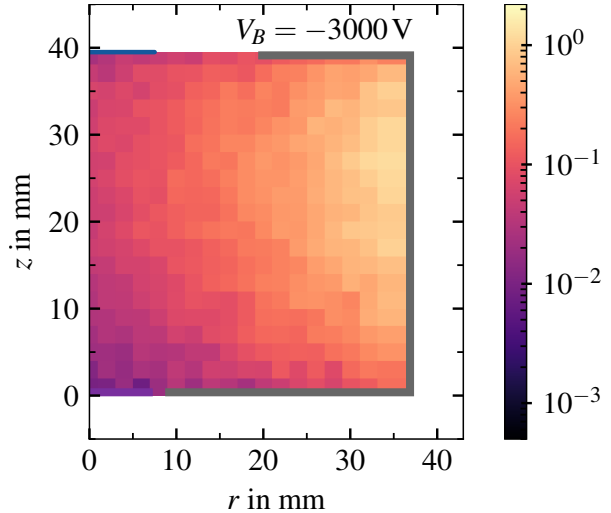


Fig. 6 Measured rate of validated two-hit events for the detector operated at -3000 V with logarithmic colorbar in counts/minute.

the side to the center of the detector is due to the absorption of outgoing gammas and the acceptance of the cameras. The measurement times were increased exponentially from 2 to 23 hours towards the center of the detector to compensate the effect. The total measurement time was about 7 days per V_B .

Data with $|V_B| < |V_D|$ were taken at -50 , -100 , -150 , -300 , -600 and -900 V. As the energy resolution of the detector deteriorates at voltages significantly below V_D , the energy measured in the detector was only used to select events but not in the determination of the z position of the Compton scatter.

The raw rates for the selected voltages are shown in the top two rows of Fig. 7. These images were calibrated using the rates as shown in Fig. 6. The results in percentage of the rate at -3000 V are shown in the bottom two rows of

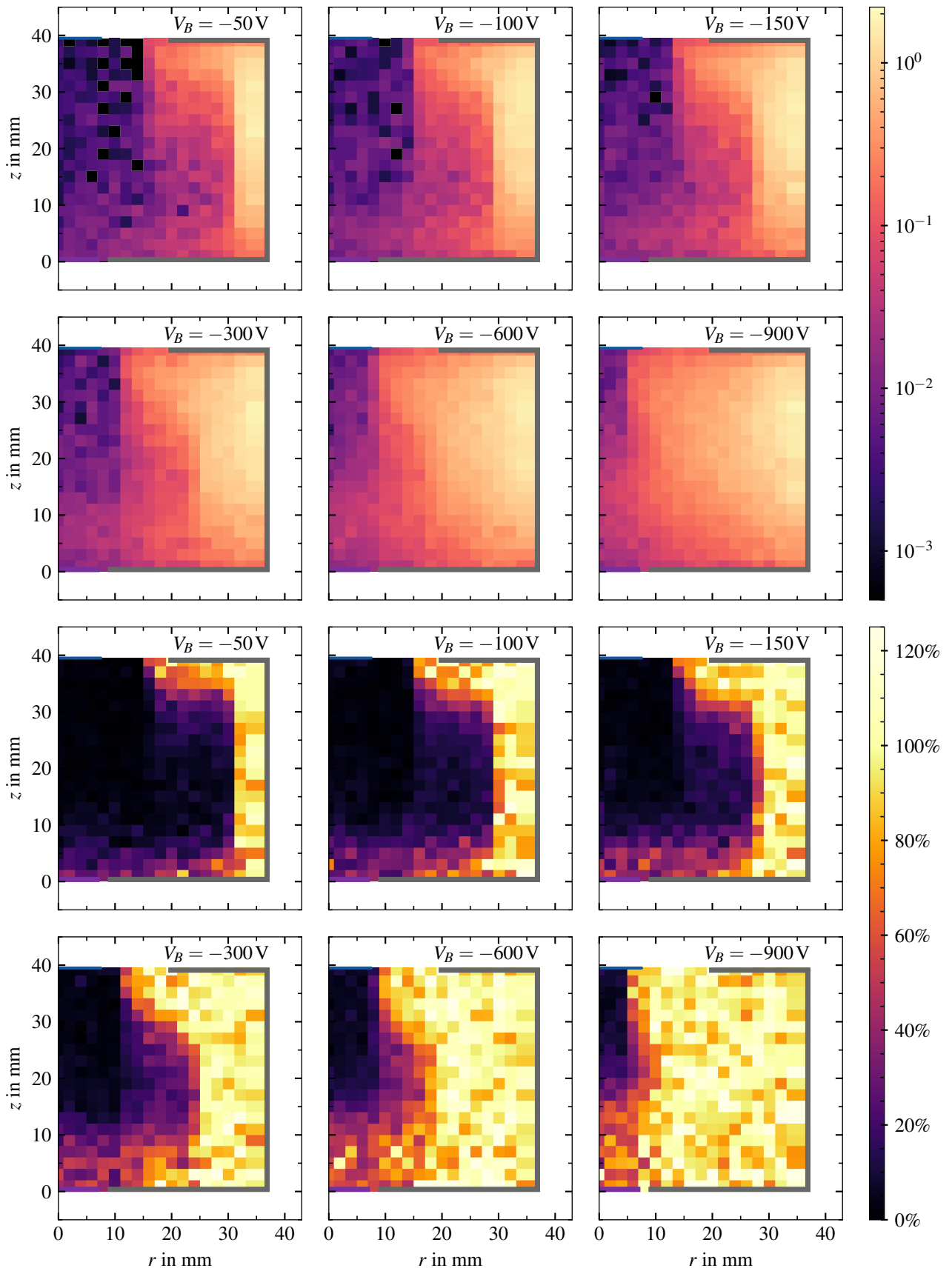


Fig. 7 Top two rows: measured rates of validated two-hit events for V_B between -50 V and -900 V with logarithmic colorbar in counts/minute. Bottom two rows: the respective rates as percentages of the rates observed at -3000 V , see Fig. 6, with linear colorbar. The range of the colorbar in the bottom rows exceeds 100 % to show the statistical fluctuations in the region with $\sim 100\%$ efficiency.

Fig. 7. These rates are relative efficiencies. Volumes with low relative efficiencies are identified as undepleted and volumes with high relative efficiency as depleted.

While the boundaries in r are well defined, the lower boundaries in z are less clearly resolved. The intrinsic resolution in z is ± 1 mm FWHM, but there are long Cauchy tails from events with large reconstruction errors [12]. At $r = 0$ mm, around half of the z -range of the detector is undepleted at $V_B = -900$ V, and more than 75 % is undepleted for V_B below -150 V. This results in a lack of events misreconstructed into the depleted volumes underneath the undepleted volumes. As event rates are generally higher at large z , see Fig. 6, the contamination with such events is expected to be higher for bins at lower z . This explains why the relative efficiencies for volumes above the undepleted volumes do not show such a significant effect. Nevertheless, the shrinkage of the undepleted volume with increasing V_B is clearly visible also in z .

Undepleted volumes were first observed while imaging a multi-kilogram inverted-coaxial point-contact germanium (IC) detector with the Compton Scanner [16]. The images presented in this paper, along with those produced for the IC detector, are the first three-dimensional images of undepleted volumes of high-purity germanium detectors³.

6 Determination of the impurity density profile from the Compton images

A well-motivated [12, p. 105] parameterization for the radial dependence of the impurity density profile in a germanium detector was found to be a hyperbolic-tangent parameterization [8, 18]. Assuming a linear z -dependence, this results in the following parameterization for the impurity density profile, ρ , of

$$\rho(r, z) = \underbrace{\left(\rho_\infty + \left(\rho_{\text{in}} \cdot \left(1 - \alpha \cdot \frac{r}{R} \right) - \rho_\infty \right) \cdot \underbrace{\frac{1}{2} \left(\tanh\left(-\frac{r - r_0}{\lambda}\right) + 1 \right)}_{\text{tanh: center at } r = r_0} \right)}_{\text{Linear } r\text{-dependence}} \cdot \underbrace{\left(1 + \beta \cdot \frac{z}{H} \right)}_{\text{Linear } z\text{-dependence}}. \quad (5)$$

Here, $R = 37.25$ mm is the radius and $H = 39.5$ mm is the height of the detector. The parameters ρ_∞ , ρ_{in} , α , r_0 , λ and β have to be determined from fits to the data. They represent the impurity density at $r \rightarrow \infty$ and $r = 0$ mm, a linear r dependence, the position of the hyperbolic-tangent component and its strength, and the relative increase in impurity density from bottom to top, respectively. It was investigated that the 12.1 % increase in impurity density provided by the manufacturer described the general behavior of the detector quite well. Thus, the value of β was fixed to 12.1 %.

³Two-dimensional projections have been reported in Ref. [17, p. 64-67].

In order to deduce the impurity density profile, a fit over all voxels with $z > 10$ mm and all bias voltages was performed using predictions from the simulation and comparing them to data. The output of the simulation was mapped onto the measured voxels. The scaling factors f introduced in section 4 for each voxel would represent the relative efficiencies for a perfect measurement. However, as the measurement was not perfect, a threshold was set and the voxel was counted as depleted, i.e. $d = 1$, or undepleted, i.e. $d = 0$, if the measured efficiency was above or below a certain percentage. The default threshold was 50 %. The loss function

$$L = \sum_{V_B} \sum_{\text{voxel}} (f(V_B) - d(V_B))^2 \quad (6)$$

was minimized with parameters restricted such that the condition $V_D = -1275$ V was fulfilled. The predictions for the borders of the undepleted volumes for the different voltages are shown in Fig. 8. The predictions for the scaled manufacturer values are also shown as well as predictions from a capacitance measurement, see section 7.

The impurity density profile as determined from the fit to the undepleted volumes is depicted in Fig. 9. The profile is provided for the top and the bottom of the detector. It is shown for the default threshold at 50 %, as well as for a threshold at 40 % and at 60 %, to identify depleted voxels. The variation of 10 % in the value of the threshold was chosen because statistical fluctuations of the order 10 % for the relative efficiency were observed in the depleted volumes, see Fig. 7. The lines intersect at $r \approx 26$ mm. This is a result of the restriction that the measured full-depletion voltage has to be reproduced. Also provided are the parameters as defined in Eq. (5) for the default threshold of 50 %.

The impurity density is almost constant for $r \lesssim 22$ mm while it drops rapidly for $r \gtrsim 22$ mm. The probed volume extends to $r \approx 30$ mm corresponding to $V_B = -50$ V, see Fig. 8. Anything beyond is an extrapolation of the fit. The probed volume ends ≈ 7 mm away from the edge of the active volume of the detector, where the n-type Lithium contact layer, see section 2, enters the calculations as 0.75 mm thick. This layer does not have a sharp edge but certainly has no influence to radii as low as 22 mm, where the impurity density starts to decrease. It drops by about one order of magnitude from $r \approx 22$ mm to the beginning of the Lithium contact.

Overall, the simulation with the impurity density profile as determined with a 50 % threshold fits the outer edge in r of the undepleted volumes very well. The predictions from the manufacturer's values scaled to 89 % with no radial dependence are also shown in Fig. 8. These predictions overestimate the radial extent of the undepleted volume for all $|V_B| < |V_D|$. This cannot be avoided without introducing a radial dependence of the impurity density. A strong decrease of the impurity density towards the edge of the detector is needed to obtain a good description of the undepleted volumes for all V_B simultaneously.

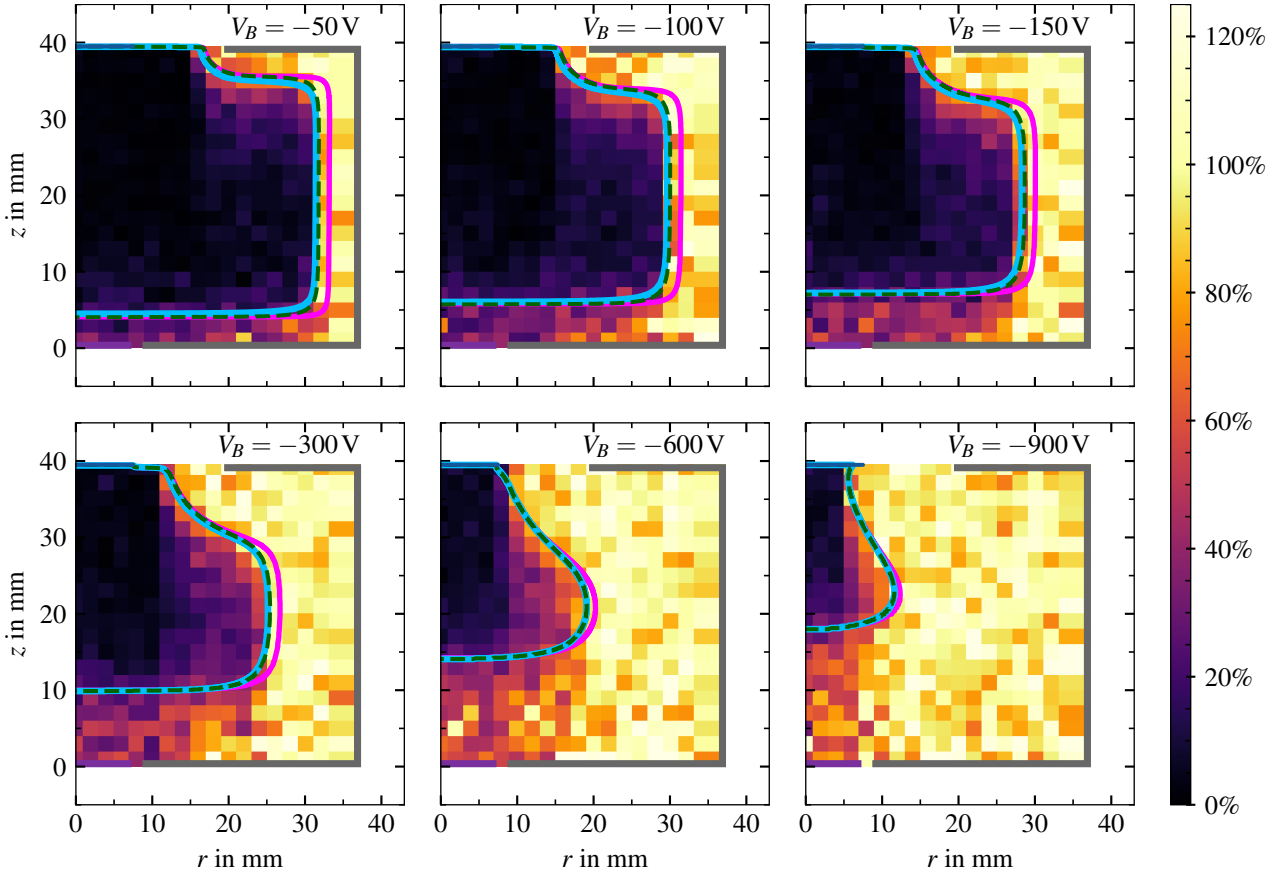


Fig. 8 Measured relative efficiencies as percentages with linear colorbar. The images are overlaid with predictions using the impurity profile from the best fit (blue line) according to Eq. (5) for a threshold of 50 % to identify a voxel as depleted. Also shown are the predictions using the impurity values provided by the manufacturer scaled to 89 % (magenta line) without a radial dependence of the impurity density profile and the predictions from the result of a fit to the capacitance curve (dashed line), see section 7.

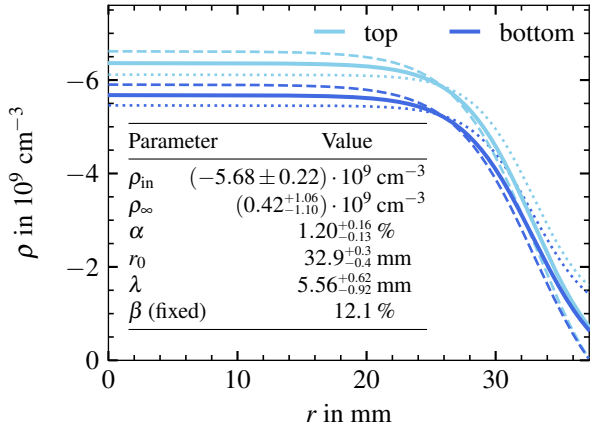


Fig. 9 Impurity density profile of the p-type segBEGe detector obtained from fits to the Compton images, using the parameterization in Eq. (5). The lines depict the best-fit results for threshold values of 50 % (solid), 40 % (dotted) and 60 % (dashed). The parameters are listed for the default threshold of 50 %.

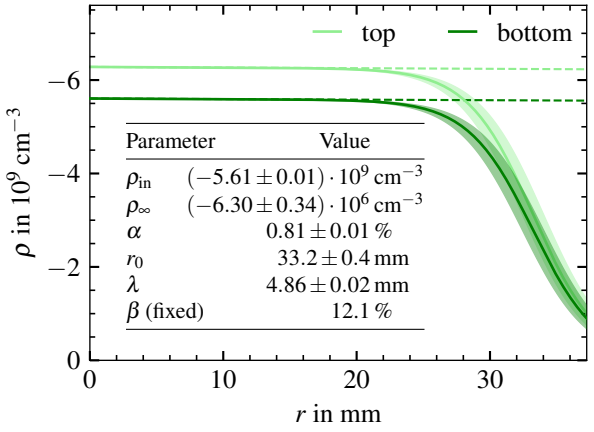


Fig. 10 Impurity density profile of the p-type segBEGe detector obtained from a maximum-likelihood fit to the measured CV-curve using the parameterization in Eq. (5). The bands indicate 2σ -uncertainties on the data. Indicated as dashed lines are the linear functions describing the impurity density profile in the central part of the detector.

7 Comparison to capacitance measurements

The capacitance of a detector, C_d , can be measured using a pulser system [8, 19]. Such a system [12, p. 97] was directly installed on the K2 cryostat housing the detector, see section 3. Figure 11 demonstrates how the detector has to be modeled to understand and calculate C_d , when it is fully or partially depleted. The depleted volume is responsible for C_d . The undepleted volume is represented by a capacitance C_u and a resistance R_u . The values of C_d in this paper were calculated with *SolidStateDetectors.jl* using the gradients of the weighting potentials [20].

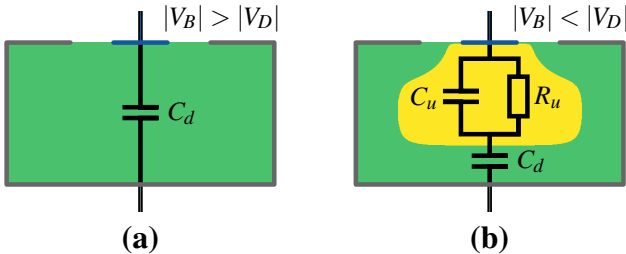


Fig. 11 Model used for the simulation of the capacitance of the p-type segBEGe detector for a (a) fully-depleted and (b) partially-depleted detector. The depleted volume is shown in green, the undepleted volume is shown in yellow.

The measured capacitance-voltage (CV) curve is shown in Fig. 12, together with the prediction using the manufacturer values scaled to 89 % as input. The scaling to 89 % adjusts the prediction to match the measured V_D . The capacitance was measured at 98 voltages down to $V_B = -120$ V, which took about 8 hours. Measurements below -120 V were outside of the operating range of the pulser system [12]. Thus, the outer region of the detector could not be probed to quite as large r as with the Compton images.

The detector capacitance C_d has a constant value for $|V_B| \geq |V_D|$. While V_D is correctly predicted for the scaled values from the manufacturer, the predictions for C_d below V_D are all above the measured values with the deviation growing with reduced V_B . This can, again, not be explained unless a radial dependence of the impurity density profile is introduced.

A maximum likelihood fit was performed to obtain the parameters of Eq. (5) with a fixed $\beta = 12.1\%$ as used for the fit to the Compton images plus the requirements of $\alpha < 1$, $0 < r_0 < R$ and $\lambda > 0$. The restriction on V_D could be omitted as V_D is determined from the voltage at which the curve becomes a constant and was extracted correctly automatically. Figure 13 shows the data together with the predicted CV curve using the best-fit impurity density profile. Also shown are the residuals of the data with respect to the 1σ and 2σ uncertainty bands on the prediction. The uncertainties are dominated by correlated systematic effects [12, p. 103]. The predictions are slightly too low between $V_B \approx -200$ V and

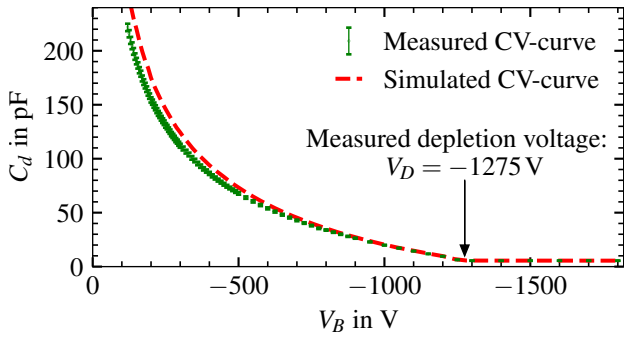


Fig. 12 Measured capacitance values (points with error bars) together with the predicted CV curve using the impurity density values from the manufacturer scaled to 89 % to match V_D (dashed red line).

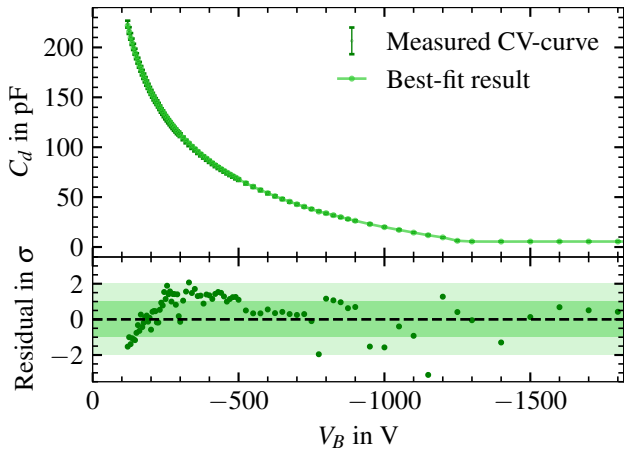


Fig. 13 Comparison of the simulated CV curve using the best-fit result according to Eq. (5) to the measured capacitance values. Also shown are the residuals for the data (green points) compared to the 1σ and 2σ uncertainty bands of the predictions.

$V_B \approx -500$ V and become too high at lower voltages. Interestingly, the radial extent of the undepleted region at around $V_B = -300$ V of $r \approx 25$ mm shown in Fig. 8 coincides with the radius at which ρ was seen to decrease.

The net impurity density profile as determined by the best fit is shown in Fig. 10. It is very similar to the profile as determined from the fit to the undepleted volumes. The uncertainty bands were calculated using the Laplace approximation. The values for ρ_{in} and ρ_{∞} agree within uncertainties. The fit uncertainties are smaller for the capacitance fit for these densities. It should, however, be remembered that ρ_{∞} comes from an extrapolation beyond the range of the data and that the capacitance fit does not probe to as large r as the fit to the Compton images. Both fits indicate that the impurity density remains almost constant for $r \lesssim 22$ mm. The values for r_0 agree within uncertainties, where both fits show similar uncertainties. This means that the downturn of impurity density sets in around $r \approx 22$ mm for both fits. The values of λ are also compatible with large uncertainties from the fit to the Compton images. In summary, the capacitance fit and the fit to the Compton images agree very well.

8 Summary and discussion

A novel method to directly image the undepleted volumes of a germanium detector was introduced and such Compton images were shown for a p-type Broad Energy germanium detector. The predictions of undepleted volumes calculated with the open-source software package *SolidStateDetectors.jl* were fitted to the images. The shape of the undepleted volumes could only be described if a radial dependence of the impurity density profile was assumed. The necessity to introduce such a radial dependence was confirmed by analyzing the capacitance-voltage curve of the detector. The impurity density profile in the center of the detector is almost constant up to a radius approximately 22 mm, where it starts to decrease rapidly. An extrapolation to the edge of the detector indicates that the net density of electrically active impurities might become very low. To our knowledge, this is the first time that three-dimensional Compton images have been produced and used to obtain the impurity density profile of a germanium detector.

Rare-event searches use pulse shape analysis to identify background events. Such an analysis can only be reliably developed from simulations for detectors with a known impurity density profile. Therefore, it is strongly suggested to measure a capacitance-voltage curve for each detector mounted in an experiment. This measurement can be completed within one day. It should be performed down to the lowest achievable voltages to probe as close to the surface as possible.

Measured capacitances represent only integrated values over the depleted volumes of the detector, limiting their capabilities to unambiguously determine individual components of the impurity density profile. The radial dependence may vary between crystal growing facilities and detector types. In addition, the assumption of a linear z -dependence might not hold for larger-height detectors. Three-dimensional Compton images of undepleted volumes would provide complementary information to disentangle radial and lateral components of the impurity density profile. The cost of a Compton Scanner as used to create the images presented in this paper is negligible compared to the cost of a large-scale germanium-based experiment. The feasibility of scanning multi-kilogram detectors has already been demonstrated. A Compton scan like the one described in this paper takes several weeks, but it seems advisable that such scans are performed for each type of detector and for each crystal growing facility.

Acknowledgements We thank our former colleagues Dr. Lukas Hauermann and Dr. Martin Schuster for helpful discussions and support.

References

1. GERDA Collaboration, Eur. Phys. J. C **284**, 82 (2022). doi:[10.1140/epjc/s10052-022-10163-w](https://doi.org/10.1140/epjc/s10052-022-10163-w)
2. MAJORANA Collaboration, Phys. Rev. C **99**, 065501 (2019). doi:[10.1103/PhysRevC.99.065501](https://doi.org/10.1103/PhysRevC.99.065501)
3. LEGEND Collaboration. LEGEND-1000 Preconceptual Design Report (2021). arXiv:[2107.11462](https://arxiv.org/abs/2107.11462)
4. SuperCDMS Collaboration, Phys. Rev. Lett. **112**, 241302 (2014). doi:[10.1103/PhysRevLett.112.241302](https://doi.org/10.1103/PhysRevLett.112.241302)
5. CDEX Collaboration, Phys. Rev. Lett. **120**, 241301 (2018). doi:[10.1103/PhysRevLett.120.241301](https://doi.org/10.1103/PhysRevLett.120.241301)
6. EDELWEISS Collaboration, Phys. Rev. Lett. **125**, 141301 (2020). doi:[10.1103/PhysRevLett.125.141301](https://doi.org/10.1103/PhysRevLett.125.141301)
7. S. Mertens, et al., Nucl. Instr. Meth. A **921**, 81 (2019). doi:[10.1016/j.nima.2018.09.012](https://doi.org/10.1016/j.nima.2018.09.012)
8. I. Abt, et al., Eur. Phys. J. C **83**, 352 (2023). doi:[10.1140/epjc/s10052-023-11509-8](https://doi.org/10.1140/epjc/s10052-023-11509-8)
9. H. Mei, D.M. Mei, G.J. Wang, G. Yang, J. Instrum. **11**(12), P12021 (2016). doi:[10.1088/1748-0221/11/12/P12021](https://doi.org/10.1088/1748-0221/11/12/P12021)
10. H. Mei, G.J. Wang, G. Yang, D.M. Mei, J. Instrum. **12**(07), P07003 (2017). doi:[10.1088/1748-0221/12/07/P07003](https://doi.org/10.1088/1748-0221/12/07/P07003)
11. I. Abt, et al., Eur. Phys. J. C **82**, 936 (2022). doi:[10.1140/epjc/s10052-022-10884-y](https://doi.org/10.1140/epjc/s10052-022-10884-y)
12. F. Hagemann, Determination of the impurity density profile and charge carrier mobilities in a point-contact germanium detector using a novel Compton Scanner. Ph.D. thesis, Technische Universität München (2024). URL <https://mediatum.ub.tum.de/?id=1741799>
13. Private communication with Mirion Technologies, Inc.
14. Private communication with D. Radford, Oakridge National Laboratory, 2025
15. I. Abt, et al., J. Instrum. **16**, P08007 (2021). doi:[10.1088/1748-0221/16/08/p08007](https://doi.org/10.1088/1748-0221/16/08/p08007)
16. D. Hervas Aguilar, Characterizing Bulk Signals in an Inverted Coaxial Point-Contact Detector to Inform Rare Event Searches. Ph.D. thesis, University of North Carolina at Chapel Hill (2023). doi:[10.17615/4xnj-1k90](https://doi.org/10.17615/4xnj-1k90)
17. S. Colosimo, The characterisation of AGATA high purity germanium detectors for pulse shape analysis. Ph.D. thesis, University of Liverpool (2013). doi:[10.17638/00011077](https://doi.org/10.17638/00011077)
18. Private communication with L. Darken, Canberra Industries, 2006
19. B. Birkenbach, et al., Nucl. Instr. Meth. A **640**(1), 176 (2011). doi:[10.1016/j.nima.2011.02.109](https://doi.org/10.1016/j.nima.2011.02.109)
20. I. Smolić, B. Klajn, Prog. Electromagn. Res. B **92**, 1 (2021). doi:[10.2528/PIERB21011501](https://doi.org/10.2528/PIERB21011501)